Title:

Multimodal Nonlinear Optical and Thermal Imaging Platform for Label-Free Characterization of Biological Tissue

Authors

Wilson R Adams,[1] Brian Mehl,[2] Eric Leiser,[2] Manqing Wang,[3] Shane Patton,[2] Graham A Throckmorton,[3] J Logan Jenkins,[3] Jeremy B Ford,[3] Rekha Gautam,[3] Jeff Brooker,[2] E. Duco Jansen,[1,4] Anita Mahadevan-Jansen[1,4,*]

Affiliations

[1]Vanderbilt University, Dept of Biomedical Engineering, Nashville, TN, 37235, USA.
[2]Thorlabs Imaging Research, Sterling, VA, USA.
[3]Chongqing University, College of Bioengineering, Chongqing, China.
[4]Vanderbilt University Medical Center, Dept of Neurosurgery, Nashville, TN, 37232, USA
* anita.mahadevan-jansen@vanderbilt.edu

Abstract

The ability to characterize the combined structural, functional, and thermal properties of biophysically dynamic samples is needed to address critical questions related to tissue structure, physiological dynamics, and disease progression. Towards this, we have developed an imaging platform that enables multiple nonlinear imaging modalities to be combined with thermal imaging on a common sample. Here we demonstrate label-free multimodal imaging of live cells, excised tissues, and live rodent brain models. While potential applications of this technology are wide-ranging, we expect it to be especially useful in addressing biomedical research questions aimed at the biomolecular and biophysical properties of tissue and their physiology.

Main Text – [4779 words]

With increased focus on high-speed biological processes at molecular, chemical, and biophysical levels, there has come a critical need to develop tools that can keep pace with the number of active research areas in biomedicine. Technical developments in nonlinear optical microscopy have revolutionized our ability to study biophysical and biochemical properties of tissues, both in terms of the wide range of samples, improved contrast modalities, and unprecedented speeds at which imaging is now possible. However, combining direct spatial temperature measurements alongside multiphoton modes of contrast have not been widely adopted. Multiphoton imaging approaches have enabled deep-tissue imaging across numerous model systems, gleaning important insights on the structure and function of cells and tissues (*1, 2*) while thermal imaging can yield complementary information to relate to study metabolism, circulation, and immune response. Temperature plays a crucial role in biology yet has yet to be extensively demonstrated in any substantial capacity towards biological microscopy applications. Thus instrumentation to explore the structural, functional, and thermal properties of tissue would prove useful in studying biophysical dynamics in tissue physiology.

Multiphoton fluorescence (MPF) and second harmonic generation (SHG), are particularly useful in highlighting tissue structure and function (*3-11*). Calcium, voltage, and molecule-sensitive reporters continue to push the boundaries of multiphoton applications in biomedical research. Vibrational spectroscopic contrast using nonlinear Raman imaging (NRI), namely coherent anti-Stoke Raman scattering (CARS) and stimulated Raman scattering (SRS), has shown particularly

wide-ranging applicability. These include rapid identification of tumor margins (*12-14*), high-dimensional structural labeling (*15, 16*), other biological processes such as drug delivery (*17-20*), biomolecular synthesis (*21, 22*), gene expression (*21*), neurotransmitter release (*23*), and electrophysiological dynamics (*24, 25*). Such imaging can highlight the molecular organization and biochemical composition of tissue over time– offering a glimpse into sub- and inter-molecular dynamics without using exogeneous labels. Multiplexing functional, biochemical, and biophysical (e.g. temperature) contrast in cells and tissues can offer a unique tool in evaluating and imaging biological and physiological processes that may not be possible with the same degree of exploratory power in separate instruments (*26-30*).

Nonlinear optical microscopy is inherently suitable for multimodal imaging applications. Integrating the different modalities that fall under nonlinear microscopy can help alleviate unnecessary system complexity while providing complementary information about tissue structure and function. Notably, CARS, SRS, MPF, and SHG are all optical processes that can occur and be detected simultaneously or sequentially by selecting the appropriate filters and detectors for the techniques used.. Several groups have demonstrated selective combinations of nonlinear imaging strategies to address a range of biological questions, *in vitro* and *in vivo*. Combined MPF and CARS microscopy has been used to study dermal structures and vasculature in nude mice ears (*31*), organelle transport in fibroblasts (*32*), and histological assessment of mammary adenocarcinoma samples (*1*), among others. Groups have also combined CARS and SHG imaging to assess damage and remyelination processes in animal models of peripheral nerve injury and neuropathy(*33-36*). The ability to sense neuronal membrane potential and calcium activity with combined SRS and calcium-sensitive MPF has been demonstrated to show the capacity of SRS for label-free sensing of neuronal action potentials (*24, 25*). Integration of SRS with optical coherence tomography (OCT) has been shown to augment nonspecific scattering-based contrast with vibrational specificity to image lipid distributions in excised human adipose tissue (*37, 38*). More recently, researchers have employed four or more nonlinear imaging modalities, including CARS, MPF, SHG, and third harmonic generation for live tissue and intravital imaging towards wound healing and cancer metastasis (*26, 27, 39*). While most of these demonstrated approaches have been applied towards observing biological processes over the span of multiple hours at the molecular and biochemical levels, they are limited in their ability to observe snapshots of sub-second functional, biochemical, and thermal processes.

The influence of temperature in physiological and biochemical processes – particularly surrounding sample damage and physiological modulation - has recently become an area of prominence across biomedical research disciplines (*40-45*). As optical imaging and perturbation technologies continue to advance biomedical research, it becomes critical to consider thermodynamic effects particularly on live specimens albeit practically difficult. A flexible imaging system that incorporates molecular, biochemical, and biophysical information from cells to tissues, *in vitro* to *in vivo,* would enable the study of rapid and dynamic biophysical processes from multiple perspectives.

Measuring temperatures in biological samples at high resolutions spatially and temporally has proven difficult and continues to be an active area of research. Groups have multiplexed blackbody thermal imaging and fluorescence microscopy at cellular resolutions *in vitro* (*30, 46, 47*), however water absorption generally obscures the ability to visualize cell morphology with thermal imaging alone. Moreover, optical components that suffice for use between 0.4 and 14 μm wavelengths to encompass visible optical and thermal infrared imaging are not readily available. Finite element heat transfer modeling and Monte Carlo simulations of photon transport

in scattering media is often regarded as the benchmark approach for temperature estimation of dynamic photothermal processes in biological samples with high water concentrations (*48-51*). Several indirect approaches have been demonstrated including temperature-dependent changes in fluorophore emission, and probe beam deflection microscopy (*43, 52-54*). While point-based methods (utilizing thermocouples, customized miniature sensors, or intrinsic fluorescence of rare-earth doped glass waveguides) are more direct, they sacrifice spatial information obtained with temperature mapping (*29, 43, 48, 55*). Translationally, thermal imaging has been applied *in vivo* towards cancer detection, circulatory diseases, and chronic pain identification (*56, 57*). However, despite the potential utility of combining thermal imaging with multimodal nonlinear microscopy, such a combination has not been previously reported. A system that can combine multimodal nonlinear microscopy with thermal imaging would offer unprecedented flexibility to study biological processes in real time.

The goal of this project is to integrate multiple nonlinear imaging methods with thermal imaging so that biophysical, biochemical, and molecular information from dynamic biological processes may be imaged with micron level spatial resolution and millisecond level temporal resolution. Towards this effort, we present an imaging platform that integrates single-band CARS, SRS, MPF, SHG, and wide field thermal microscopy (ThM) for characterizing tissues at varying time scales. Applications of our imaging system are demonstrated imaging both *in vitro* with neural cell cultures and tissue specimen as well as *in vivo* with acute craniotomy rat preparations. Our platform offers a novel approach enabling imaging techniques with otherwise incompatible optical paths (due to physical limitations of hardware) to be applied on a common sample. We demonstrate that this platform provides a robust tool for researchers to probe the physiology of dynamic biological systems, through the unique integration of vibrational spectroscopic, functional fluorescence, and thermal contrast.

System Design

The framework of the Multimodal Advanced Nonlinear and Thermal Imaging System, or MANTIS, is a three-armed imaging turret (Customized Bergamo II Platform, Thorlabs Imaging Research, Sterling, VA, USA) that respectively images a sample with either nonlinear imaging, thermal imaging, or widefield white light reflectance imaging which is reconfigurable to adapt additional measurement approaches (Figure 1A). The mechanical arrangement of distinct imaging arms allows for modalities with incompatible optical instrumentation (e.g. ultrafast near infrared imaging with endogenous shortwave infrared measurements) to be performed sequentially without disturbing or repositioning the sample. A FLIR SC8300-series high-speed indium-antimonide CCD camera equipped with a 4X germanium imaging objective (FLIR Systems Inc., Nashua, NH, USA | Figure 1B) is attached to the thermal imaging arm of the microscope. The thermal camera relies on the endogenous black/grey body emission of a sample between 3-5µm wavelength under the assumption of homogenous emissivity to infer sample temperatures.

The nonlinear imaging section of MANTIS, depicted in Figure 1C with a simplified schematic, is coupled to two nonlinear laser sources supplying femtosecond (Insight DS+, Spectra Physics, Fremont, CA, USA) and picosecond (picoEmerald S, A.P.E, Berlin, DE) laser lines. Higher spectral bandwidth (~15nm) femtosecond laser pulses provides high peak powers necessary for optimal multiphoton and higher harmonic generation *in vivo* (*2, 58*). The picosecond laser has narrower bandwidth (~0.5nm, or $10cm^{-1}$), which is critical for maintaining the spectral resolution necessary for single-band nonlinear Raman imaging while minimizing power at the sample for safe *in vivo* applications (<20mW average power) (*59, 60*). Both laser

systems operate with a pulse repetition rate of 80MHz and output two beams necessary for pump and stokes excitation of NRI contrast processes. The shorter wavelength tunable laser line undergoes a tunable path length delay while the longer wavelength laser line is intensity-modulated at 20MHz via an electro-optical modulator (Thorlabs, Newton, NJ, USA) to facilitate SRS. Each laser's output is spatially and temporally co-linear and directed with a series of mirrors into the scan head of the nonlinear imaging arm of MANTIS.

The imaging optics of the nonlinear imaging arm are based on conventional upright laser-scanning microscopy. The scanning optics consist of a pair of galvanometric mirrors (Thorlabs, Newton, NJ, USA), which are imaged onto the back focal plane of a commercial objective lens (Olympus XLUMPLFLN, 20X 1.0NA | Nikon CFI Apochromat NIR 60X, 1.0NA) via a 4f optical relay. This scan relay performs a fixed 4X magnification of the laser beam diameter to accommodate the back-aperture pupil size of the largest objective lenses we use relative to the entrance beam diameter (SL50-2P2 & TL200-2P2, Thorlabs, Newton, NJ, USA). Two epi-detection ports with a photomultiplier tube (CARS/MPF/SHG | GaAsP Amplified PMT, Thorlabs, USA) and a large area 50-V reverse-biased photodiode (SRS | A.P.E. GmbH, Berlin, DE) are used for imaging epi-detected contrast. Two additional detachable forward detection ports were also built to accommodate coherent imaging modalities in transparent samples in transmission mode. Stimulated Raman loss for SRS was demodulated via a commercial lock-in-amplifier (A.P.E. Gmbh, Berlin, DE). All emission filters and excitation wavelengths included with the system are summarized in Table S1 (Semrock, Brattleboro, VT, USA). Scanning and detection hardware for imaging is controlled through ThorImageLS version 2.1, 3.0, or 3.2 (Thorlabs Imaging Research, Sterling, VA, USA). All images shown are raw with linear intensity rescaling, with all analysis being performed in FIJI (*61*).

The third imaging arm of MANTIS initially features a color complementary metal oxide semiconductor (CMOS) camera (Thorlabs Inc., Newton, NJ, USA) with a variable focal length lens (Navitar Inc., Rochester, NY, USA) for widefield white-light reflectance imaging of samples (Figure 1A). However this arm was built into the imaging system to readily enable integration of additional contrast modalities that may be further incompatible with multimodal nonlinear microscopy – such as interferometric contrast or stereoscopic surgical guidance. Each arm is locked into position by a custom-designed spring-loaded locking system against the rotating turret base (Figure 1A). The maximum fields of view of each imaging arm is ~800µm-x-800µm for nonlinear microscopy with a 20X objective, 3mm-x-4mm for thermal microscopy with a 4X objective, and 50mm-x-50mm for widefield white light reflectance imaging.

System Performance

To achieve high-speed imaging at subcellular resolution, MANTIS was designed to resolve at least 1-µm lateral resolution in the nonlinear imaging arm. Performance was verified on a series of standards, (Fig. **2**), with measured axial and lateral resolutions for each modality summarized in Table S2 (data summarized in Table S1). Images of 0.5-µm diameter polystyrene (PS, latex, Polysciences Inc. Warrington, PA, USA) beads with CARS and SRS were obtained to generate a point spread function (PSF), which is reported here as the full-width half-maximum intensity cross-section of beads fit to a Gaussian curve. Fluorescent bead calibration standards with a 250-nm diameter (Polysciences Inc. Warrington, PA, USA) were used to measure the PSF of MPF. All PSF calculations were performed using the MetroloJ plugin in FIJI (*61, 62*). Measured resolutions, reported in Table S2, are on par with results published literature when imaging with numerical apertures approaching 1.0. Spectral separation of polymethyl-methacrylate (PMMA, acrylic, Polysciences Inc. Warrington, PA, USA)) and PS beads with single-band SRS are shown

181 in Fig. **2**B. Acrylic (PMMA) beads are depicted using the 2927-cm^{-1} band – an asymmetric CH_3
182 resonance- (yellow), and latex (PS) beads are depicted spectrally separate with the 3053-cm^{-1}
183 band– an asymmetric CH_2 resonance- in blue. The signal-to-noise ratio (SNR), measured at the
184 edge of a vegetable oil meniscus at the 2927-cm^{-1} band with SRS (Figure S2), was calculated to
185 be 34.6 (*63*).
186 Resolution standards to verify SHG imaging resolution are not commercially available. In
187 place of a controlled standard, a collagen-rich biological sample (a porcine mitral valve) was
188 imaged at a high spatial sampling density (250-nm/px) and the finest resolvable fibrillar
189 structures were measured as a proxy for lateral resolution. Sample images of mitral valve
190 collagen are shown in Fig. **2**E and Figure S3. Example calculations of fibril diameter are show in
191 Figure S1. Fibrillar collagen bundles and quaternary structure are clearly visualized. While
192 fibrillar structures vary substantially in diameter (*64*), the resolving power of SHG on MANTIS
193 (Table 2) is well within our targeted resolution goals being able to resolve sub-micron spatial
194 features.
195 The FLIR thermal camera resolution was estimated by identifying the smallest resolvable
196 group on a 1951 United States Air Force resolution target. Resolving group 6, element 4 equates
197 to a lateral resolution of 6.9-µm. The axial resolution of the thermal camera was estimated to be
198 around 20-µm, which is substantially larger than the depth of field of the nonlinear imaging arm,
199 making registration in the axial dimension straightforward. Factory measured temperature
200 resolution is specified to be 0.1°C. Registration of the nonlinear and thermal microscopy field
201 view were centrally registered to the corner of a 10-um grid target. Switching between thermal
202 and nonlinear microscopy fields of view was found to repeatable within 1-µm radial to imaging
203 turret rotation and 10-µm tangent to imaging turret rotation (Figure 1A, yellow arrows). Since
204 field of view of the thermal camera is nearly four times that of the nonlinear microscopy field of
205 view – making the coincidence of each modality's field of view with each other straight-forward
206 Figure S5. Once aligned, the fields of view were observed to remain well registered for more
207 than a week following initial alignment. It takes about 90-180 seconds to switch between
208 nonlinear and thermal imaging arms over the same sample. The sub-millimeter repeatability of
209 positioning multiple imaging arms readily enables multiplexing of thermal and nonlinear
210 microscopy on the same field of view without needing to reposition the sample.

211 **in vitro Imaging**
212 To verify the capability of MANTIS to perform *in vitro* imaging label-free, cultured NG108 cells
213 – a spiking neuron-astrocytoma hybridoma cell line - were imaged with CARS and MPF, as seen
214 in Fig. **3**. Performing CARS imaging at 2830-cm^{-1} resonance highlights a lipid-dominant CH_2
215 asymmetric stretch mode, which relates to cellular projections and lipid-rich intracellular
216 contents such as organelles, lipid droplets, and vesicles (Fig. **3**A). Autofluorescence from NADH
217 and FAD reveals metabolic information about relative aerobic metabolism dynamics and
218 metabolic cofactor distribution throughout the cell – demonstrating the structural and functional
219 capacities of multimodal nonlinear imaging *in vitro* (Fig. **3**B and C). Blackbody thermal imaging
220 of cells in media in an upright configuration was not feasible due to the strong absorption of
221 water in the wavelength range measured by the thermal camera (3 to 5-µm). Imaging with
222 cellular resolution with thermal microscopy is possible in an upright configuation (Figure S4A),
223 with the ability to resolve cellular temperature distribution. However, once medium is introduced
224 to the imaging field of view (Figure S4B), cellular morphology is occluded due to strong water
225 absorption of the sensed wavelength range. This has been addressed by others by utilizing

inverted imaging configurations (*29, 30, 46*) , however resolvable cellular morphology was not demonstrated.

Combined SHG and MPF was demonstrated on fresh *ex vivo* porcine mitral valve samples (Figure S5). Autofluorescence and SHG under 930-nm illumination with the femtosecond laser source yielded high resolution microstructure of endogenous elastin and collagen, free of exogenous labeling (*3*). Changes in collagen and elastin can dangerously disrupt the structure and function of heart valves (*65, 66*). Having methods to study new interventions to improve heart valve function could be valuable to cardiac biomechanics researchers. Combining SHG with SRS at 2880-cm^{-1} to broadly highlight lipids allows for the visualization of tissue architecture in unfixed frozen sections of murine cervix (Figure S6). Distinct chemical and structural differences are notable between the epithelium and stroma of the cervix. The stroma is dense with collagen and low in cellular content, while the epithelium is rich in lipids and proteins due to cellularization. The lamina propria of blood vessels are also discernable with SHG, appearing as fine tubular structures with strong SHG signal, providing an indication of tissue vascularization. Visualizing the changes in vasculature, cellular, extracellular matrix protein distribution throughout cervix shows potential for studying parturition processes and cancer progression in the cervix without the need for exogenous labelling.

Fig. **4**, Figure S6, and Figure S7 demonstrate multimodal nonlinear imaging with CARS, SRS, SHG, and MPF in an ex vivo rat sciatic nerve preparation. Contrast from CARS and SRS primarily highlights myelin (Figure S7B&C). The CARS and SRS images correspond well with the MPF images of FluoroMyelin green (ThermoFisher Inc | Figure S7E, Figure S8C and D) but are less prone to heterogeneous dye uptake in exogenously stained tissue. While myelin plays a major functional role in nerve signal conduction, collagen is a major structural component of the sciatic nerve providing a protective exterior sheath and additional mechanical stability within the nerve. Collagen contrast from SHG can be used to visualize the epineurium and fascicle-residing collagen (Figure S9). These four modalities together therefore offer key structural insight to the sciatic nerve and can be used to study nerve injury, regeneration, and disease.

The key advancement allowed by the MANTIS platform is the ability to multiplex optically incompatible imaging techniques such as thermal imaging with nonlinear optical microscopy. Thermal imaging can be used to evaluate fast photothermal processes, such as infrared neural stimulation (*48, 55, 67*), with coregistered contrast from nonlinear imaging modalities to study real time biophysical dynamics. To assess the multimodal capabilities of MANTIS, readout of multimodal nonlinear contrast was directly correlated with high-speed temperature changes during infrared neural stimulation in a fresh *ex vivo* sciatic nerve preparation (Fig. **4**). Point-scanned line repeats were employed to obtain high framerate nonlinear signals during IR stimulation. Intriguingly, our results show a notable decrease in nonlinear signals that tracks closely with temperature increases over the period of one second. Notably, SHG signals did not exhibit a discernable decrease in signal, which is attributable to the lack of collagen present through where line scans were acquired (center of the field of view, Fig. **4**). However, decreases in SHG signal during IR stimulation have been verified in other FOVs, suggesting this signal decrease is a more general physical phenomenon. Decreases in nonlinear signal were found to be caused by a defocusing artifact induced by the thermal gradient inherent to infrared neural stimulation in the field of view. Resolving photothermal effects of IR heating in biological tissues at high speed, such as during INS, will provide invaluable information in studying *in vivo* applications of INS.

in vivo Imaging

An acute craniotomy preparation in an anesthetized rat model was utilized to validate the *in vivo* capabilities of MANTIS. All animal use protocols were approved by Vanderbilt University Institute for Animal Care and Use Committee (VU-IACUC). Pixel dwell times needed to be increased to 8-µs to account for signal loss in moving the SRS detection path into an epi-detection configuration. Images were initially acquired at a high spatial sampling density (0.5-µm/px, 800x800 px) with a 0.2Hz framerate. However, reducing the spatial sampling density and overall image sizes (3µm/px, 256x256 px) over a comparable field of view, we were able to achieve 2Hz framerates. Subsequently, repeated point-based line scanning could be implemented with a 488Hz line rate to observe faster biophysical dynamics. This flexibility emphasizes the trade-offs between spatial and temporal sampling in nonlinear microscopy approaches *in vivo*. Acquiring images using CARS, MPF, or SHG needed to be performed sequentially, due to the availability of only one PMT detector at the time of experiments. However, any one of the three PMT-requiring modalities can be multiplexed with SRS contrast, since SRS uses a separate detector in an adjacent detection path.

Examples of *in vivo* images can be seen in Fig. **5**. A lipid-rich CARS resonance at 2850cm^{-1} (Fig. **5**C) and a protein-dominant SRS resonance at 2930cm^{-1} (Fig. **5**B) highlights superficial cellular features, as well as vascular perfusion within blood vessels. Autofluorescence contrast of endogenous NADH (Fig. **5**G) and FAD (Fig. **5**E) reveal additional metabolic information, where FAD signal appears more punctate across the brain surface while NADH signal appears more diffuse. This diffuse contribution from NADH is likely from the neuropil at the pial surface of the cortex, while FAD tends to be confined to the somatic portions of cells that occupy outer layers of the cortex in lower abundance, concurrent with observations *in vitro* and *in vivo* (*68, 69*). Contrast from SHG (Fig. **5**F) revealed unknown morphologies, which may be due to cytoskeletal structures across the pial surface (*2, 70*) or residual collagen from the dura mater left behind following surgical preparation. Thermal imaging (Fig. **5**H) shows clear topographical morphologies of the brain surface, with vessels clearly visible. The lack of optical penetration depth of measured wavelengths of the thermal camera are likely responsible for the brain surface topographical contrast (*71*). Temperature fluctuations across the surface of the brain appear to be minimal, even with breathing, heart rate, and motion artifacts. Larger vessels appear slightly warmer than smaller vessels. Focusing artifacts appeared to have some effect on the accurate approximation of the brain surface temperature within 1°C – particularly noticeable at the edges of the field of view (Fig. **5**H). Cellular morphologies were not apparent in thermal images of the brain surface. Thermal imaging of the brain surface was capable of acquisition speeds approaching 180Hz framerates with a full field of view. This imaging rate can be substantially increased to 500Hz or more by cropping the image sensor without loss in spatial resolution, or pixel binning without reduction in field of view. The vessel morphologies visible between thermal and CARS/SRS contrast made fine registration of thermal and nonlinear imaging fields straightforward with rigid registration.

Discussion

We demonstrate the first imaging system that combines CARS, SRS, MPF, SHG, and thermal imaging into a single microscope for biomedical imaging. The similarities in illumination and detection instrumentation needed for nonlinear excitation has been exploited in the past to design multimodal imaging platforms. But as demonstrated here, our novel system design includes a movable turret that allows for overlaying these different modalities to achieve a more complete picture of biological processes to be imaged. This implies that any other imaging modality that

typically could not be integrated into a nonlinear optical microscopy path may be similarly incorporated. Such flexibility of optical microscopy design provides the opportunity to study physiology in unique and dynamic ways.

The proposed imaging system, MANTIS, was built with modularity and expandability in mind. On the nonlinear imaging arm, the current configuration has four optional detection ports - two each in the epi- and forward detection configurations. Additional channels can easily be added to expand simultaneous imaging capabilities based on research needs. Lock-in detection arms can be refitted with the appropriate optical filters for transient absorption imaging (*72*). Sum-frequency generation imaging can also be readily integrated for studying ordered molecular orientation and interfacial phenomena in biological samples (*73*). The widefield reflectance imaging arm may be useful for integrating laser speckle, diffuse reflectance, optical coherence tomography and microscopy, or spatial frequency domain imaging with the correct illumination optics to map tissue blood flow, oxygenation, and optical properties. Furthermore, the widefield reflectance and thermal imaging arm were built on detachable 96-mm optical rails so that other imaging methods may be integrated based on future research needs.

The scanning optics used in nonlinear imaging arm can achieve 1kHz scan rates. A galvo-scanning pair was chosen over a faster galvo-resonant scanning pair, which typically offer an order of magnitude increase in scanning rates. By doing so, improved control could be achieved over image sampling densities that span subcellular and multicellular scales. This is exemplified by the difference in sampling density observed between Fig. **3** and Fig. **5**. As demonstrated in Fig. **4**, our imaging system can perform nonlinear imaging with line scans approaching 0.5kHz with detectable amounts of signal. This is enough to resolve high-speed biophysical dynamics, such as during neural modulation or optogenetic stimulation, from a functional, chemical, and physical standpoint, as demonstrated in Fig. **4**. Kilohertz bandwidth scanning rates are sufficient to achieve visualization of neuronal action potentials as demonstrated by Lee *et al.* with balanced detection SRS and calcium fluorescence microscopy (*24*).

Both femtosecond and picosecond lasers were included in the design of MANTIS for signal and spectral resolution considerations. The bandwidth of the picosecond laser source (around 0.5nm) allows for higher spectral resolutions (around $10cm^{-1}$) which is critical for nonlinear Raman imaging (*59, 74*). However, the peak powers of the picosecond source are orders of magnitude lower than that of the femtosecond laser, yielding less contrast during multiphoton fluorescence and higher harmonic imaging. At the time of construction, the use of broadband nonlinear Raman techniques, such as pulse shaping and spectral focusing had yet to be realized for fast imaging *in vivo* (*75-78*). As such, design considerations to optimize narrow band spectral resolution and *in vivo* imaging speed were a priority. A number of broadband spectral NRI techniques have since been described (*79-83*), with a handful demonstrated *in vivo* (*83-88*). The flexibility of the existing instrumentation on MANTIS readily allows us to integrate such broadband approaches into MANTIS with expanded optical configurations.

Using blackbody thermal microscopy to characterize sample temperatures in conjunction with nonlinear imaging, or any laser-scanning microscopy approach, has yet to be previously published. Estimating temperature with a thermal camera provides a more direct measurement than other approaches, such as fluorescence-based methods. The ability to measure thermal information alongside the functional and structural information offered by nonlinear microscopy provides a unique instrument to explore new questions in biophysics, particularly *ex vivo* and *in vivo*. Practically, thermally microscopy presents some advantages and drawbacks depending on

the model systems being imaged. We have found that high resolution fluorescence microscopy can be difficult to interpret in highly thermally dynamic systems with high numerical apertures at high imaging speeds, which became apparent in applying infrared neural stimulation in sciatic nerve (Fig. **4**) as well as cells. Having thermal information to contrast and systematically compensate for thermally-induced effects is something that our imaging platform lends itself well to accomplish. Since imaging depth with thermal microscopy is limited due to the optical penetration depth of water in the 3-5µm wavelength spectral regime, this means that SWIR based imaging methods are ideally suited for measuring surface temperatures in water-dominant samples such as biological tissues. This is even more apparent *in vitro*, where imaging through any amount of aqueous medium occludes sample morphology (Figure S4). While others have demonstrated blackbody thermal imaging of cells via inverted microscopy through cover glass (*29, 30, 46, 47*), visualizing cell morphology with thermal imaging has not been previously demonstrated. Thermal microscopy on MANTIS can be performed readily and reliably on tissues *ex vivo* (Fig. **4**F) and *in vivo* (Fig. **5**H). Topographical features such as blood vessels tissue surfaces are clearly visible. The pronounced topography of these anatomical features is helpful when performing fine registration nonlinear and thermal imaging fields. This capability of thermal imaging is analogous to the operating principles of microscopy with ultraviolet surface excitation (MUSE) (*71*), where the shallow penetration depth of SWIR light in water (~10µm) enables temperatures measurements and topographical contrast in the most superficial portions of tissue being imaged. Temperature at aqueous interfaces are useful in approximating spatial temperature distributions *in vitro*. Combining surface temperatures with finite element heat transfer modeling and precise control over sample thermodynamics can be used to render volumetric estimates of temperature *in vitro* (*47*). In combination with fluorescence or other nonlinear imaging modalities, imaging the thermodynamics of adherent cells *in vitro* or in tissues with thermal microscopy could be quite useful. Consequently, multimodal methods almost become an essential requirement to correlate temperature and real-time cellular observations. Our microscopy platform readily allows such observation to be made and flexibly configured to address a wide range of biological and physiological questions.

Conclusion

We present a novel and flexible multimodal optical imaging system that combines nonlinear and thermal microscopies for biomedical imaging. Our platform can be used to overlay functional, structural, and biochemical information from a single specimen tracked over time at high speed and spatial resolution. Such approaches can be applied to study dynamic biophysical processes in cells and tissues, *in vitro* and *in vivo*. In conjunction with continually expanding molecular biology tools, this instrument and related imaging methods will aid in studying physiological and biochemical processes from multiple perspectives in many fields including neuroscience, cancer biology, metabolic disease, tissue biomechanics, and much more.

Supplemental Materials

Table S1: Summary of emission filters and excitation wavelengths used for multimodal imaging. All filters obtained from Semrock (Brattleboro, VT, USA).
Table S2: Summary of measured system resolutions across multiple imaging modalities.
Table S3: Detailed summary of point spread function calculations for nonlinear imaging modalities.

Figure S1: Sample Lateral Resolution Characterization for SHG imaging in a porcine mitral valve sample. Gaussian fitting performed in FIJI.

Figure S2: Signal to Noise calculation with a Vegetable Oil meniscus in FIJI. SNR was calculated to be 34.6.

Figure S3: To-scale representation of the overlap of multimodal imaging fields of view for the 3 imaging arms of MANTIS.

Figure S4: Thermal images of cultured 3T3 Fibroblasts. A) Cells imaged without any aqueous medium. B) Image of aqueous medium front advancing over cells. The absorption of water in the short-wave infrared is high, making cell culture medium difficult to image through with blackbody thermal contrast.

Figure S5: Porcine Mitral Valve imaging with endogenous autofluorescence from elastin (left) and collagen SHG (right). Image width is 520-µm.

Figure S6: Simultaneous SHG (cyan) and SRS (2880-cm-1, lipid dominant resonance, orange) imaging of an unstained murine cervix unfixed frozen section. The stroma (dense in collagen) and epithelium are easily discernable based on relative concentrations on ratio of SHG and SRS signals. Blood vessels lamina propria are also visible with SHG contrast.

Figure S7: Composite multimode image of an ex vivo rat sciatic nerve. (A) CARS signal at 2927cm-1 (B, green), SRS signal at 2927cm-1 (C, red), SHG signal (D, cyan), and multiphoton fluorescence of FluoroMyelin Green (E, Grey). All scale bars are 100um.

Figure S8: Ex vivo rat sciatic nerve samples imaged with multimodal nonlinear imaging from Supp. Fig. X. Two different modalities can be combined in different ways to visualize tissue structure.

Figure S9: Supplementary Figure 9: Ex vivo rat sciatic nerve samples imaged with SRS (red, myelin at 2927cm-1) and SHG (cyan, collagen). Rescaled SHG images are shown to highlight intrafasicular collagen, which is in lower abundance and overall signal then epineurial collagen.

References

1. S. Yue, M. N. Slipchenko, J. X. Cheng, Multimodal Nonlinear Optical Microscopy. *Laser Photon Rev* **5**, (2011).
2. W. R. Zipfel, R. M. Williams, W. W. Webb, Nonlinear magic: multiphoton microscopy in the biosciences. *Nat Biotechnol* **21**, 1369-1377 (2003).
3. K. Tilbury *et al.*, Second harmonic generation microscopy analysis of extracellular matrix changes in human idiopathic pulmonary fibrosis. *Journal of biomedical optics* **19**, 086014 (2014).
4. P. J. Campagnola *et al.*, Three-dimensional high-resolution second-harmonic generation imaging of endogenous structural proteins in biological tissues. *Biophysical journal* **82**, 493-508 (2002).
5. A. J. Walsh *et al.*, Quantitative optical imaging of primary tumor organoid metabolism predicts drug response in breast cancer. *Cancer Res* **74**, 5184-5194 (2014).
6. A. J. Walsh, M. C. Skala, Optical metabolic imaging quantifies heterogeneous cell populations. *Biomedical optics express* **6**, 559-573 (2015).
7. T. M. Heaster, A. J. Walsh, Y. Zhao, S. W. Hiebert, M. C. Skala, Autofluorescence imaging identifies tumor cell-cycle status on a single-cell level. *Journal of biophotonics* **11**, (2018).
8. S. L. Best *et al.*, Collagen organization of renal cell carcinoma differs between low and high grade tumors. *BMC Cancer* **19**, 490 (2019).
9. T. N. Thimm, J. M. Squirrell, Y. Liu, K. W. Eliceiri, B. M. Ogle, Endogenous Optical Signals Reveal Changes of Elastin and Collagen Organization During Differentiation of Mouse Embryonic Stem Cells. *Tissue Eng Part C Methods* **21**, 995-1004 (2015).
10. C. Stosiek, O. Garaschuk, K. Holthoff, A. Konnerth, In vivo two-photon calcium imaging of neuronal networks. *Proc Natl Acad Sci U S A* **100**, 7319-7324 (2003).
11. F. Helmchen, W. Denk, Deep tissue two-photon microscopy. *Nature Methods* **2**, 932-940 (2005).
12. J. R. Linzey *et al.*, Rapid Intraoperative Diagnosis of Sellar Region Tumors Using Stimulated Raman Histology. *J Neurol Surg B* **80**, A140 (2019).
13. D. A. Orringer *et al.*, Rapid intraoperative histology of unprocessed surgical specimens via fibre-laser-based stimulated Raman scattering microscopy. *Nature Biomedical Engineering* **1**, 0027 (2017).
14. M. Ji *et al.*, Detection of human brain tumor infiltration with quantitative stimulated Raman scattering microscopy. *Science Translational Medicine* **7**, 309ra163-309ra163 (2015).
15. F. Hu *et al.*, Supermultiplexed optical imaging and barcoding with engineered polyynes. *Nat Methods* **15**, 194-200 (2018).
16. L. Wei *et al.*, Super-multiplex vibrational imaging. *Nature*, (2017).
17. C. S. Liao *et al.*, Microsecond scale vibrational spectroscopic imaging by multiplex stimulated Raman scattering microscopy. *Light-Science & Applications* **4**, 9 (2015).
18. M. Lee, W. J. Tipping, A. Serrels, A. N. Hulme, V. G. Brunton. (2017), vol. 10069, pp. 100690T-100690T-100698.
19. S. You *et al.*, Intracellular imaging of docosanol in living cells by coherent anti-Stokes Raman scattering microscopy. *Journal of biomedical optics* **22**, 70502 (2017).
20. S. Osseiran *et al.*, Characterizing stratum corneum structure, barrier function, and chemical content of human skin with coherent Raman scattering imaging. *Biomedical optics express* **9**, 6425-6443 (2018).

21. L. Wei *et al.*, Live-Cell Bioorthogonal Chemical Imaging: Stimulated Raman Scattering Microscopy of Vibrational Probes. *Accounts of chemical research*, (2016).
22. L. Wei *et al.*, Imaging Complex Protein Metabolism in Live Organisms by Stimulated Raman Scattering Microscopy with Isotope Labeling. *ACS chemical biology*, (2015).
23. D. Fu, W. Yang, X. S. Xie, Label-free Imaging of Neurotransmitter Acetylcholine at Neuromuscular Junctions with Stimulated Raman Scattering. *J Am Chem Soc*, (2016).
24. H. J. Lee *et al.*, Label-Free Vibrational Spectroscopic Imaging of Neuronal Membrane Potential. *The journal of physical chemistry letters*, 1932-1936 (2017).
25. B. Liu *et al.*, Label-free spectroscopic detection of membrane potential using stimulated Raman scattering. *Applied Physics Letters* **106**, 173704 (2015).
26. S. You *et al.*, Intravital imaging by simultaneous label-free autofluorescence-multiharmonic microscopy. *Nat Commun* **9**, 2125 (2018).
27. H. Tu *et al.*, Concurrence of extracellular vesicle enrichment and metabolic switch visualized label-free in the tumor microenvironment. *Science Advances* **3**, (2017).
28. Q. Luo *et al.*, Hyperspectral-stimulated Raman scattering imaging of cholesteryl ester accumulation: new avenue to diagnosis of human prostate cancer. **10024**, 100241M (2016).
29. T. Y. Choi *et al.*, Thermal evaluation of laser exposures in an in vitro retinal model by microthermal sensing. *Journal of biomedical optics* **19**, 97003 (2014).
30. M. L. Denton *et al.*, Spatially correlated microthermography maps threshold temperature in laser-induced damage. *Journal of biomedical optics* **16**, 1-12, 12 (2011).
31. C. L. Evans *et al.*, Chemical imaging of tissue in vivo with video-rate coherent anti-Stokes Raman scattering microscopy. *Proc Natl Acad Sci U S A* **102**, 16807-16812 (2005).
32. X. Nan, E. O. Potma, X. S. Xie, Nonperturbative chemical imaging of organelle transport in living cells with coherent anti-stokes Raman scattering microscopy. *Biophysical journal* **91**, 728-735 (2006).
33. T. B. Huff *et al.*, Real-time CARS imaging reveals a calpain-dependent pathway for paranodal myelin retraction during high-frequency stimulation. *PLoS One* **6**, e17176 (2011).
34. Y. Shi *et al.*, Longitudinal in vivo coherent anti-Stokes Raman scattering imaging of demyelination and remyelination in injured spinal cord. *Journal of biomedical optics* **16**, 106012 (2011).
35. T. B. Huff, J. X. Cheng, In vivo coherent anti-Stokes Raman scattering imaging of sciatic nerve tissue. *Journal of Microscopy-Oxford* **225**, 175-182 (2007).
36. Y. Fu, H. Wang, T. B. Huff, R. Shi, J. X. Cheng, Coherent anti-Stokes Raman scattering imaging of myelin degradation reveals a calcium-dependent pathway in lyso-PtdCho-induced demyelination. *J Neurosci Res* **85**, 2870-2881 (2007).
37. F. E. Robles, K. C. Zhou, M. C. Fischer, W. S. Warren, Stimulated Raman scattering spectroscopic optical coherence tomography. *Optica* **4**, 243 (2017).
38. F. E. Robles *et al.*, Coherently broadened, high-repetition-rate laser for stimulated Raman scattering-spectroscopic optical coherence tomography. *Optics letters* **44**, 291-294 (2019).
39. S. A. Boppart *et al.*, Label-free optical imaging technologies for rapid translation and use during intraoperative surgical and tumor margin assessment. *Journal of biomedical optics* **23**, 021104 (2017).
40. S. F. Owen, M. H. Liu, A. C. Kreitzer, Thermal constraints on in vivo optogenetic manipulations. *Nat. Neurosci.* **22**, 1061-1065 (2019).
41. J. B. Azimzadeh, B. A. Fabella, N. R. Kastan, A. J. Hudspeth, Thermal Excitation of the Mechanotransduction Apparatus of Hair Cells. *Neuron* **97**, 586-595 e584 (2018).

42. A. Picot *et al.*, Temperature Rise under Two-Photon Optogenetic Brain Stimulation. *Cell Rep* **24**, 1243-1253 e1245 (2018).
43. K. Podgorski, G. Ranganathan, Brain heating induced by near-infrared lasers during multiphoton microscopy. *J Neurophysiol* **116**, 1012-1023 (2016).
44. R. Palankar *et al.*, Nanoplasmonically-induced defects in lipid membrane monitored by ion current: transient nanopores versus membrane rupture. *Nano letters* **14**, 4273-4279 (2014).
45. R. Liljemalm, T. Nyberg, H. von Holst, Heating during infrared neural stimulation. *Lasers in surgery and medicine* **45**, 469-481 (2013).
46. M. L. Denton *et al.*, Effect of ambient temperature and intracellular pigmentation on photothermal damage rate kinetics. *Journal of biomedical optics* **24**, 1-15, 15 (2019).
47. A. J. Walsh, G. P. Tolstykh, S. Martens, B. L. Ibey, H. T. Beier, Action potential block in neurons by infrared light. *Neurophotonics* **3**, 040501 (2016).
48. J. B. Ford *et al.*, Identifying the Role of Block Length in Neural Heat Block to Reduce Temperatures During Infrared Neural Inhibition. *Lasers in surgery and medicine* **0**, (2019).
49. E. Marchandise, A. Mouraux, L. Plaghki, F. Henrotte, Finite element analysis of thermal laser skin stimulation for a finer characterization of the nociceptive system. *Journal of neuroscience methods* **223**, 1-10 (2014).
50. B. Choi, a. J. Welch, Analysis of thermal relaxation during laser irradiation of tissue. *Lasers in surgery and medicine* **29**, 351-359 (2001).
51. M. Ganguly, M. W. Jenkins, E. D. Jansen, H. J. Chiel, Thermal block of action potentials is primarily due to voltage-dependent potassium currents: a modeling study. *Journal of Neural Engineering* **16**, 036020 (2019).
52. A. J. Walsh, D. B. Masters, E. D. Jansen, A. J. Welch, A. Mahadevan-Jansen, The effect of temperature on the autofluorescence of scattering and non-scattering tissue. *Lasers in surgery and medicine* **44**, 712-718 (2012).
53. D. Moreau, C. Lefort, R. Burke, P. Leveque, R. P. O'Connor, Rhodamine B as an optical thermometer in cells focally exposed to infrared laser light or nanosecond pulsed electric fields. *Biomedical optics express* **6**, 4105-4117 (2015).
54. L. M. Maestro *et al.*, CdSe Quantum Dots for Two-Photon Fluorescence Thermal Imaging. *Nano letters* **10**, 5109-5115 (2010).
55. M. G. Shapiro, K. Homma, S. Villarreal, C. P. Richter, F. Bezanilla, Infrared light excites cells by changing their electrical capacitance. *Nat Commun* **3**, 736 (2012).
56. E. F. Ring, K. Ammer, Infrared thermal imaging in medicine. *Physiol Meas* **33**, R33-46 (2012).
57. G. A. Wallace, N. Singh, E. Quiroga, N. T. Tran, The Use of Smart Phone Thermal Imaging for Assessment of Peripheral Perfusion in Vascular Patients. *Ann Vasc Surg* **47**, 157-161 (2018).
58. C. Xu, W. Zipfel, B. S. Jason, R. M. Williams, W. W. Webb, Multiphoton Fluorescence Excitation: New Spectral Windows for Biological Nonlinear Microscopy. *Proceedings of the National Academy of Sciences of the United States of America* **93**, 10763-10768 (1996).
59. C. Y. Lin *et al.*, Picosecond spectral coherent anti-Stokes Raman scattering imaging with principal component analysis of meibomian glands. *Journal of biomedical optics* **16**, 021104 (2011).
60. C. W. Freudiger *et al.*, Label-Free Biomedical Imaging with High Sensitivity by Stimulated Raman Scattering Microscopy. *Science* **322**, 1857-1861 (2008).

570 61. J. Schindelin *et al.*, Fiji: an open-source platform for biological-image analysis. *Nat*
571 *Methods* **9**, 676-682 (2012).
572 62. C. C. Matthews, Fabrice P. . (2006).
573 63. D. Zhang, M. N. Slipchenko, J. X. Cheng, Highly Sensitive Vibrational Imaging by
574 Femtosecond Pulse Stimulated Raman Loss. *The journal of physical chemistry letters* **2**, 1248-
575 1253 (2011).
576 64. P. Campagnola, Second harmonic generation imaging microscopy: applications to
577 diseases diagnostics. *Analytical chemistry* **83**, 3224-3231 (2011).
578 65. M. Prunotto, P. P. Caimmi, M. Bongiovanni, Cellular pathology of mitral valve prolapse.
579 *Cardiovasc Pathol* **19**, e113-117 (2010).
580 66. R. A. Levine *et al.*, Mitral valve disease--morphology and mechanisms. *Nat Rev Cardiol*
581 **12**, 689-710 (2015).
582 67. J. Wells *et al.*, Biophysical mechanisms of transient optical stimulation of peripheral
583 nerve. *Biophysical journal* **93**, 2567-2580 (2007).
584 68. E. Stuntz *et al.*, Endogenous Two-Photon Excited Fluorescence Imaging Characterizes
585 Neuron and Astrocyte Metabolic Responses to Manganese Toxicity. *Sci Rep* **7**, 1041 (2017).
586 69. M. A. Yaseen *et al.*, Fluorescence lifetime microscopy of NADH distinguishes alterations
587 in cerebral metabolism in vivo. *Biomedical optics express* **8**, 2368-2385 (2017).
588 70. A. C. Kwan, K. Duff, G. K. Gouras, W. W. Webb, Optical visualization of Alzheimer's
589 pathology via multiphoton-excited intrinsic fluorescence and second harmonic generation. *Optics*
590 *express* **17**, 3679-3689 (2009).
591 71. A. Qorbani *et al.*, Microscopy with ultraviolet surface excitation (MUSE): A novel
592 approach to real-time inexpensive slide-free dermatopathology. *J Cutan Pathol* **45**, 498-503
593 (2018).
594 72. H. Wang *et al.*, In vivo coherent Raman imaging of the melanomagenesis-associated
595 pigment pheomelanin. *Sci Rep* **6**, 37986 (2016).
596 73. A. M. Hanninen, R. C. Prince, R. Ramos, M. V. Plikus, E. O. Potma, High-resolution
597 infrared imaging of biological samples with third-order sum-frequency generation microscopy.
598 *Biomedical optics express* **9**, 4807-4817 (2018).
599 74. C. W. Freudiger *et al.*, Stimulated Raman Scattering Microscopy with a Robust Fibre
600 Laser Source. *Nat Photonics* **8**, 153-159 (2014).
601 75. D. Fu, G. Holtom, C. Freudiger, X. Zhang, X. S. Xie, Hyperspectral imaging with
602 stimulated Raman scattering by chirped femtosecond lasers. *The journal of physical chemistry. B*
603 **117**, 4634-4640 (2013).
604 76. I. Rocha-Mendoza, W. Langbein, P. Borri, Coherent anti-Stokes Raman
605 microspectroscopy using spectral focusing with glass dispersion. *Applied Physics Letters* **93**,
606 201103 (2008).
607 77. T. Hellerer, A. M. K. Enejder, A. Zumbusch, Spectral focusing: High spectral resolution
608 spectroscopy with broad-bandwidth laser pulses. *Applied Physics Letters* **85**, 25-27 (2004).
609 78. C. Zhang, D. Zhang, J. X. Cheng, Coherent Raman Scattering Microscopy in Biology and
610 Medicine. *Annu Rev Biomed Eng*, (2015).
611 79. R. He *et al.*, Stimulated Raman scattering microscopy and spectroscopy with a rapid
612 scanning optical delay line. *Optics letters* **42**, 659-662 (2017).
613 80. C. E. Dedic, T. R. Meyer, J. B. Michael, Single-shot ultrafast coherent anti-Stokes Raman
614 scattering of vibrational/rotational nonequilibrium. *Optica* **4**, 563 (2017).

81. J. V. Thompson *et al.*, Single-shot chemical detection and identification with compressed hyperspectral Raman imaging. *Optics letters* **42**, 2169-2172 (2017).
82. C. H. Camp, Jr. *et al.*, High-Speed Coherent Raman Fingerprint Imaging of Biological Tissues. *Nat Photonics* **8**, 627-634 (2014).
83. S. Satoh *et al.*, Label-free visualization of acetaminophen-induced liver injury by high-speed stimulated Raman scattering spectral microscopy and multivariate image analysis. *Pathology international* **64**, 518-526 (2014).
84. M. Ogawa *et al.*, Label-free biochemical imaging of heart tissue with high-speed spontaneous Raman microscopy. *Biochem Biophys Res Commun* **382**, 370-374 (2009).
85. E. Capitaine *et al.*, Fast epi-detected broadband multiplex CARS and SHG imaging of mouse skull cells. *Biomedical optics express* **9**, 245-253 (2018).
86. F. K. Lu *et al.*, Label-free DNA imaging in vivo with stimulated Raman scattering microscopy. *Proc Natl Acad Sci U S A* **112**, 11624-11629 (2015).
87. H. J. Lee *et al.*, Assessing cholesterol storage in live cells and C. elegans by stimulated Raman scattering imaging of phenyl-Diyne cholesterol. *Sci Rep* **5**, 7930 (2015).
88. D. Zhang, P. Wang, M. N. Slipchenko, J. X. Cheng, Fast vibrational imaging of single cells and tissues by stimulated Raman scattering microscopy. *Accounts of chemical research* **47**, 2282-2290 (2014).

Funding
Funding for this work was provided by the following grants: AFOSR DURIP FA9550-15-1-0328, AFOSR FA9550-14-1-0303, AFOSR FA 9550-17-1-0374. WRA was supported through the ASEE NDSEG Fellowship.

Acknowledgements
The authors would also like to thank Dr. Bryan Millis, Dr. Christine O'Brien, and Dr. Andrea Locke for their feedback and guidance on the manuscript. The authors would also like to thank Dr. Matthew Bersi, Joshua Bender, and Dr. W David Merryman for providing the porcine mitral valve samples.

Author Contributions
AMJ, EDJ, and JB conceived the idea for the manuscript. WRA, BM, EL, SP, JB and AMJ designed, and built the imaging system. AMJ and EDJ secured funding support for the published work. MW performed *in vivo* surgical preparations and assisted in imaging. RG, GT, JLJ, and JBF provided samples and experimental guidance imaging tissue samples. WRA assisted in all sample preparations, performed all imaging experiments, image processing, data analysis, and prepared the manuscript. All authors contributed to editing manuscript.

Conflicts of Interest Statement
BM, EL, SP, and JB are employees of Thorlabs Imaging Research, LLC. The remaining authors report no additional conflicts of interest.

Figures

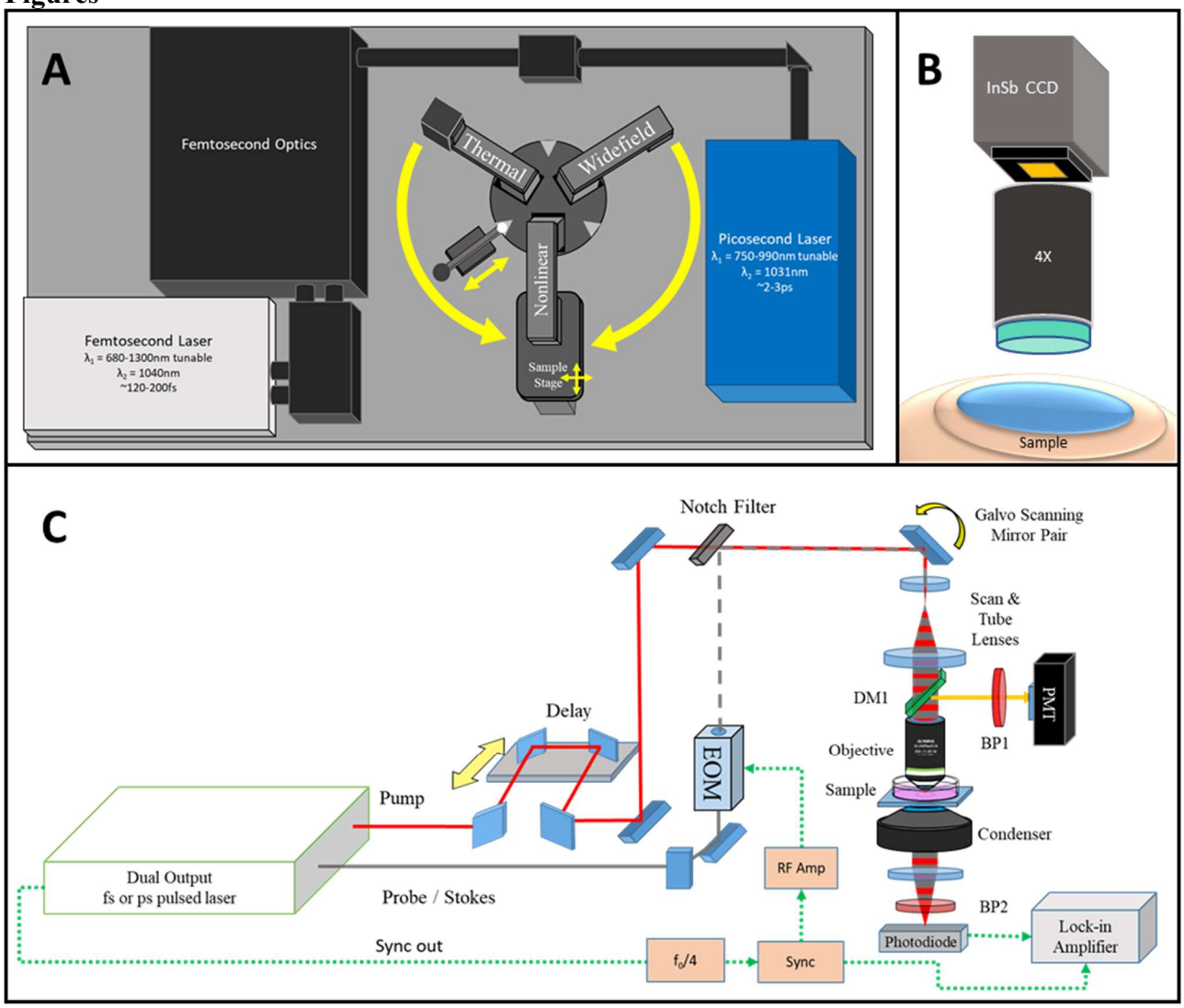

Fig. 1: MANTIS System Design. A) The layout of MANTIS. Capable of performing multimodal nonlinear and thermal imaging over the same sample. Additionally, white light imaging on a third imaging arm is available for further expansion of the system. B) Schematic of wide-field thermal microscopy, which infers the temperature of a sample based on the blackbody emission observed between wavelengths of 3 and 5µm. C) General optical schematic of a multimodal nonlinear imaging system capable of integrating CARS, SRS, MPF and SHG imaging. DM – dichroic mirror, BP – bandpass filter, PMT – photomultiplier tube, EOM – electro-optical modulator, InSb CCD – indium antimonide charge coupled device.

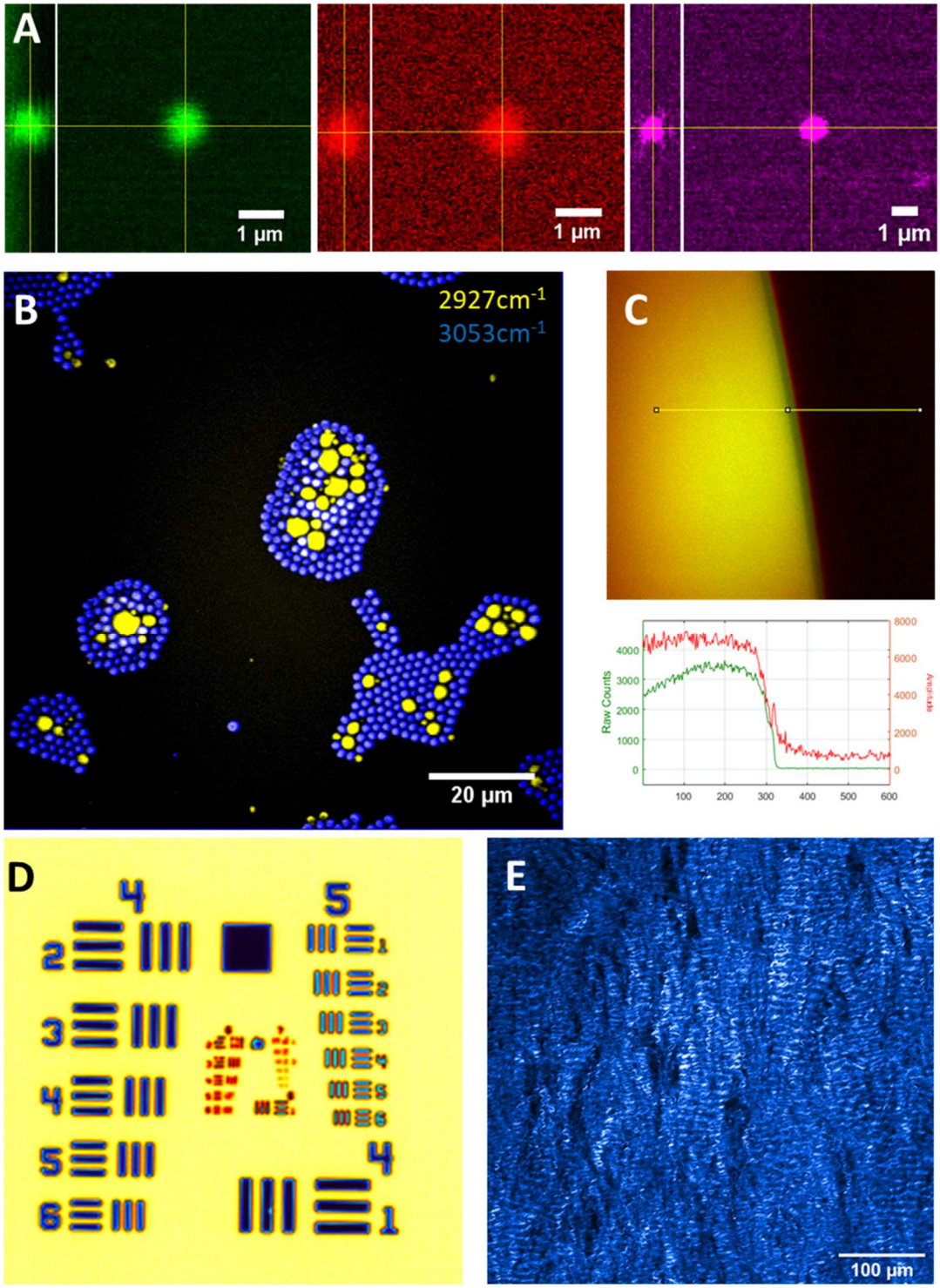

Fig. 2: MANTIS System Performance. A) Resolution of CARS (Green), SRS (Red) with a 1µm polystyrene bead, and Multiphoton Fluorescence (Magenta) with a 500-nm yellow-fluorescent polystyrene bead. Measured resolutions summarized in Table S1. B) Preparation of mixed beads containing 2µm polystyrene beads (blue, 2927cm^{-1}) with 1-10µm PMMA beads (yellow, 3053cm^{-1}). Peaks specific to each bead type C) CARS (Green) and SRS (Red) of signal-to-noise profile measured at

a vegetable oil – air meniscus at 2927cm^{-1}. D) Thermal Imaging of a 1951 U.S. Air Force Target. E) SHG imaging of a porcine mitral valve ex vivo.

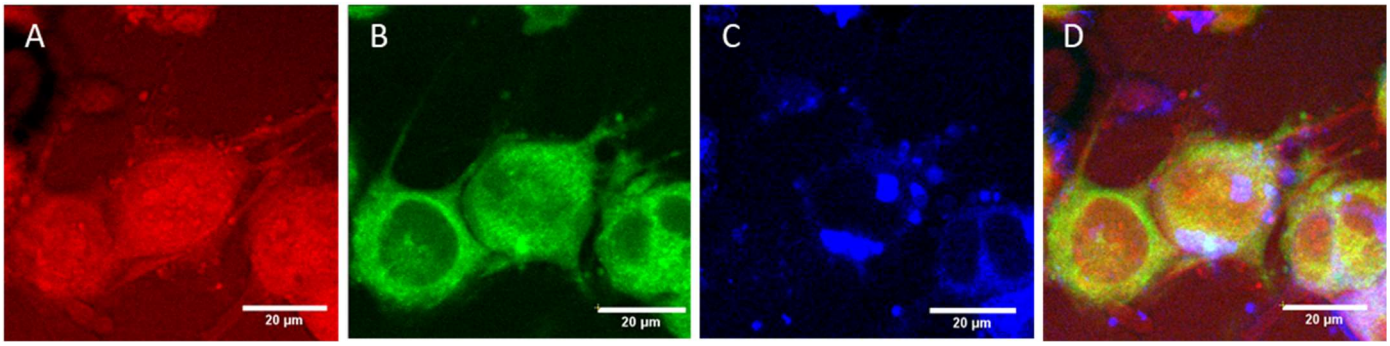

Fig. 3: *in vitro* imaging capabilities of MANTIS. NG108 cells observed with CARS (A) at 2830cm^{-1}, a protein-dominant peak, NADH autofluorescence (B), FAD autofluorescence (C), and as a composite overlay of the three channels (D). Images were acquired separately and coregistered together with a rigid transformation.

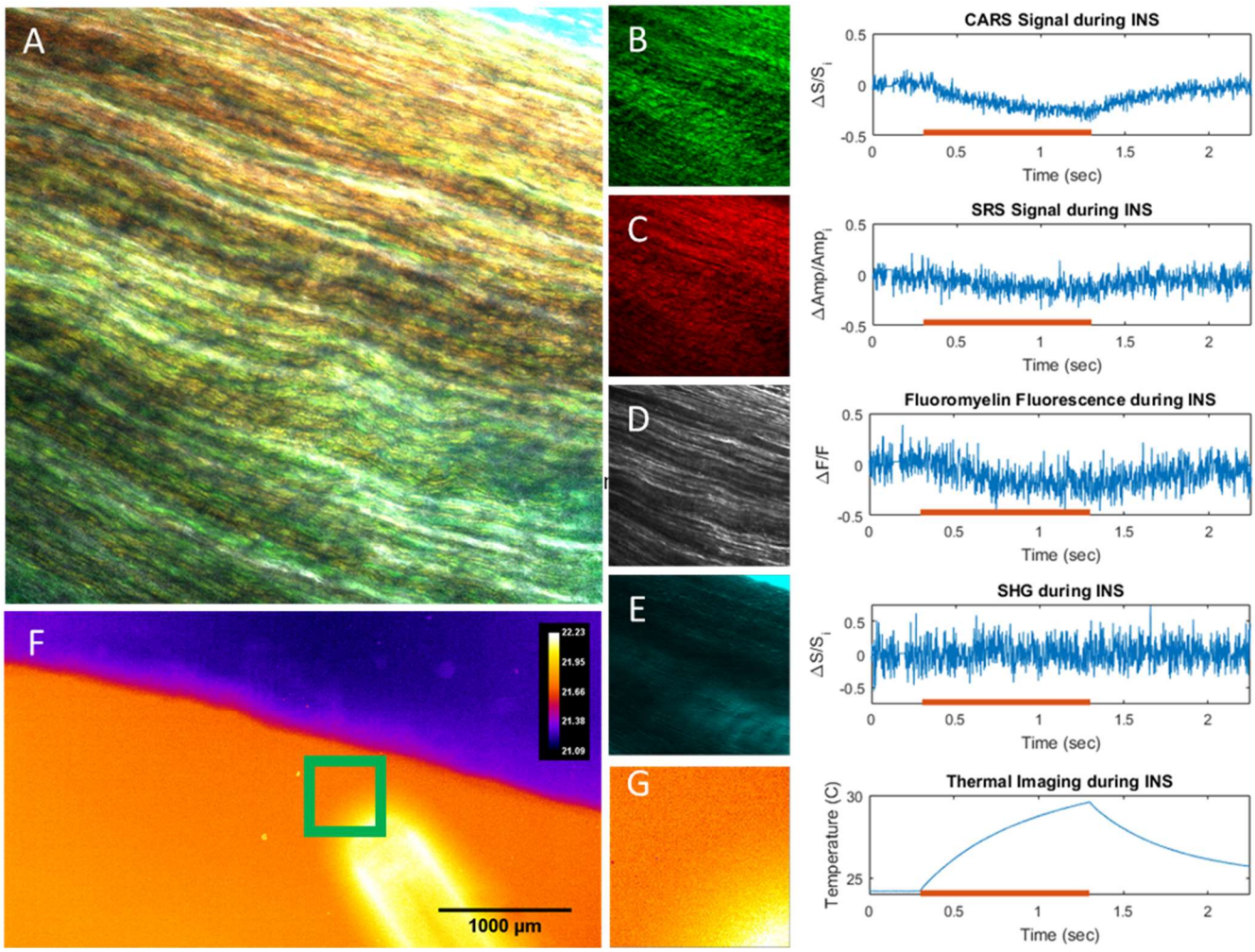

Fig. 4: Ex vivo rat sciatic nerve samples imaged with high-speed multimodal nonlinear and thermal microscopy. A) Combined image of B-E. Images and corresponding high-speed line scans through the centers of the fields of view with B) CARS at 2880-cm^{-1}. C) SRS at 2880cm^{-1}, D) Fluoromyelin Green, E) SHG. Red lines on graphs indicate the exposure of the tissue to 1875nm light from an optical fiber. Light exposure causes a local temperature increase over 1 second (thermal images, F& G) yielding a corresponding decrease in nonlinear signals.

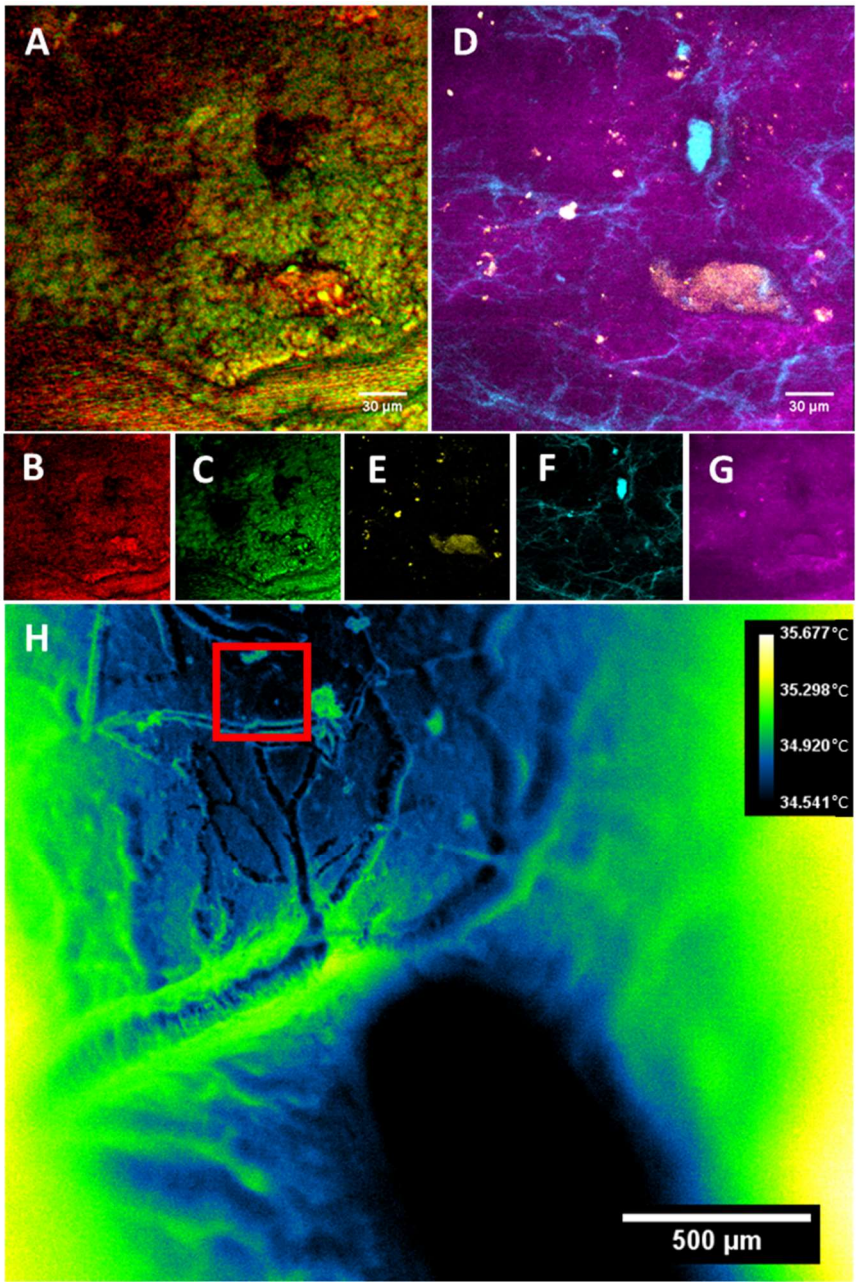

Fig. 5: Multimodal images from a rat brain in vivo. A) Composite image of B (SRS, 2930cm^{-1}) and C (CARS, 2850cm^{-1}) highlighting lipid and protein-dominated signals, respectively. D) Composite image of the same field of view in A of E (FAD autofluorescence), F (SHG signal), and G (NADH autofluorescence). (H) Thermal images of the brain surface, temperatures shown in °C.

Tables

Table S1: Summary of emission filters and excitation wavelengths used for multimodal imaging. All filters obtained from Semrock (Brattleboro, VT, USA).

Contrast	Filter (Center/Passband FWHM)	Excitation Wavelengths
CH-band CARS	625nm/90nm	792-803nm & 1040nm
SRS	890nm/310nm	792-803nm & 1040nm
NADH/Blue Fluorescence	460nm/30nm	780nm
FAD/Green Fluorescence	525nm/30nm	934nm

Table S2: Summary of measured system resolutions across multiple imaging modalities.

Modality	Lateral Resolution (µm)	Axial Resolution (µm)
CARS	0.632	3.009
SRS	0.833	3.136
MPF	0.359	1.502
SHG	0.388	X
Thermal	6.9	X

Table S3: Detailed summary of point spread function calculations for nonlinear imaging modalities.

CARS						
					Mean	STD
x	0.646	0.615	0.636	**x**	**0.6323**	0.0158
y	0.773	0.69	0.772	**y**	**0.7450**	0.0476
z	2.758	3.282	2.986	**z**	**3.0087**	0.2627
SRS						
x	0.849	0.743	0.906	**x**	**0.8327**	0.0827
y	0.896	0.793	0.86	**y**	**0.8497**	0.0523
z	3.36	2.813	3.235	**z**	**3.1360**	0.2866
MPF						
x	0.379	0.272	0.426	**x**	**0.3590**	0.0789
y	0.286	0.413	0.377	**y**	**0.3587**	0.0655
z	1.473	1.432	1.601	**z**	**1.5020**	0.0882
SHG						
L	0.388	0.383	0.433	**L**	**0.4013**	0.0275

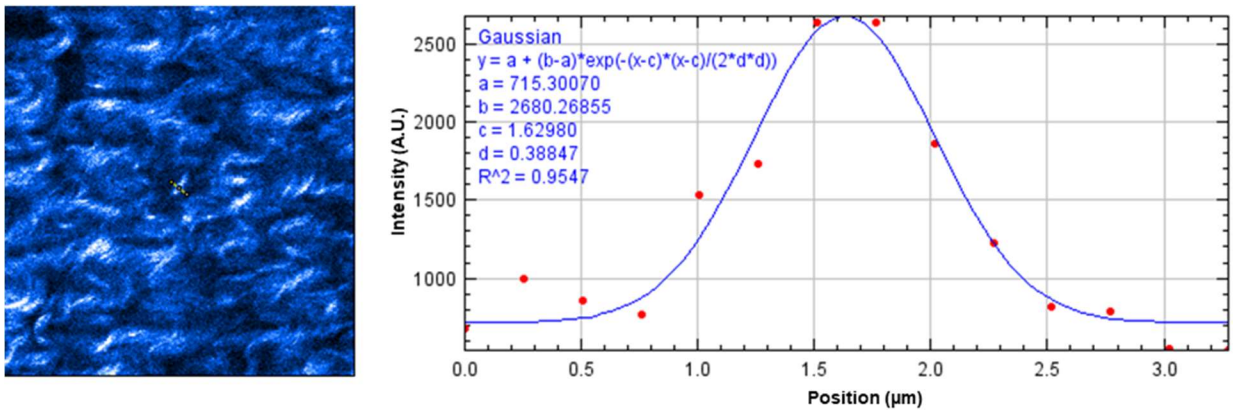

Figure S1: Sample Lateral Resolution Characterization for SHG imaging in a porcine mitral valve sample. Gaussian fitting performed in FIJI.

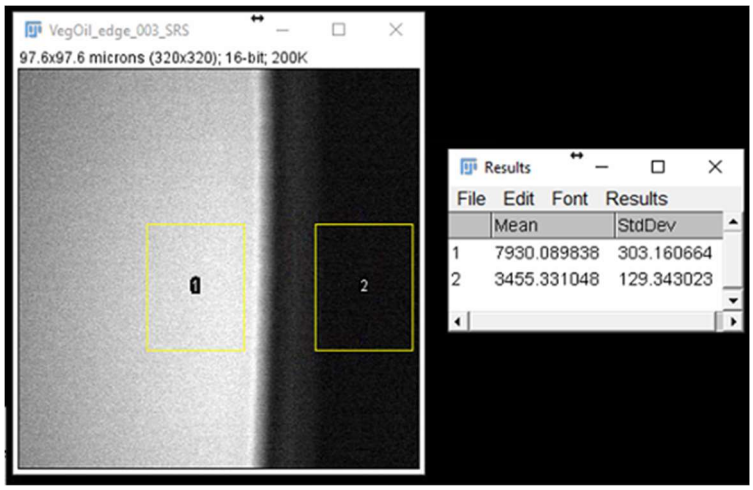

Figure S2: Signal to Noise calculation with a Vegetable Oil meniscus in FIJI. SNR was calculated to be 34.6.

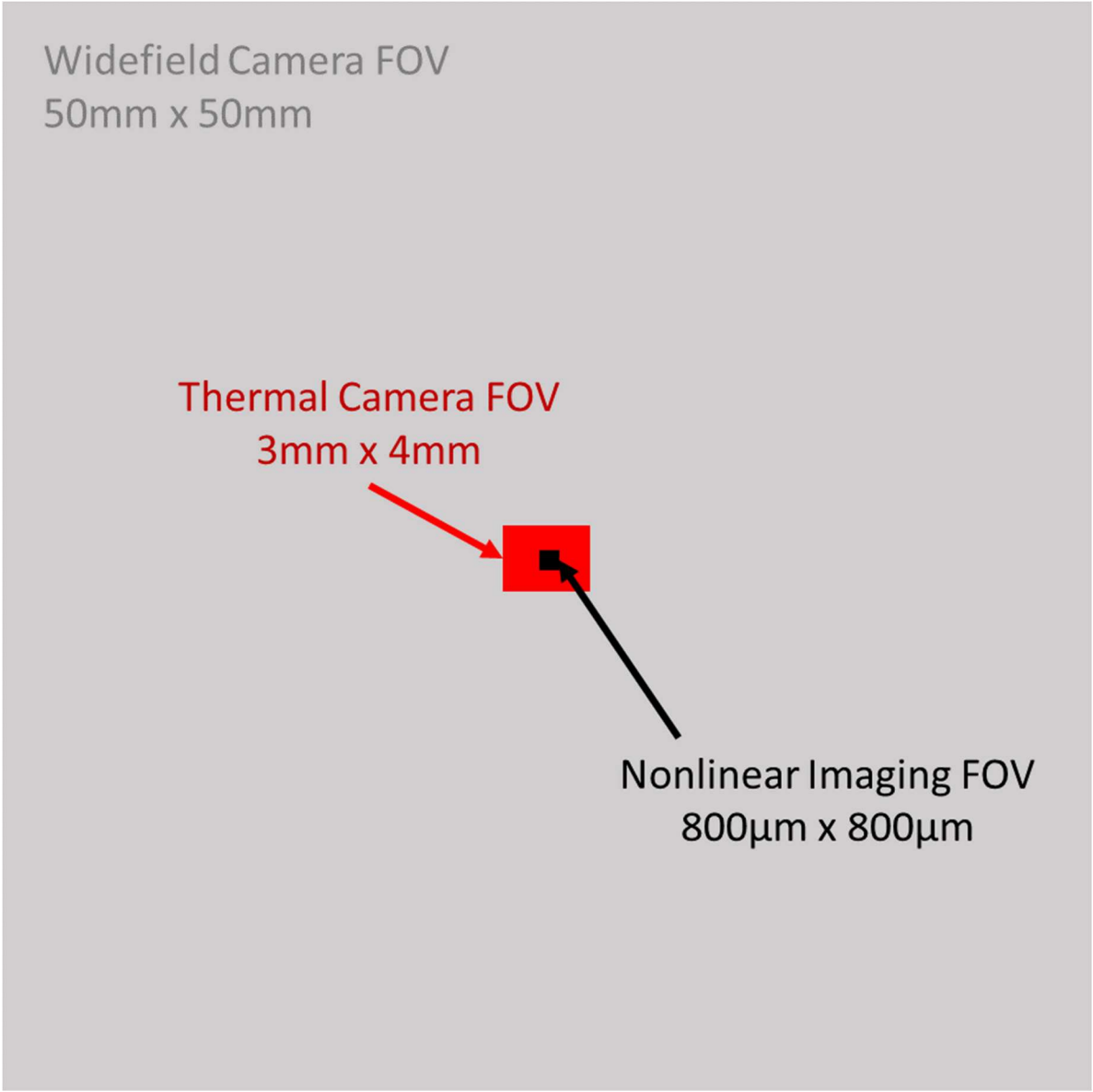

Figure S3: To-scale representation of the overlap of multimodal imaging fields of view for the 3 imaging arms of MANTIS.

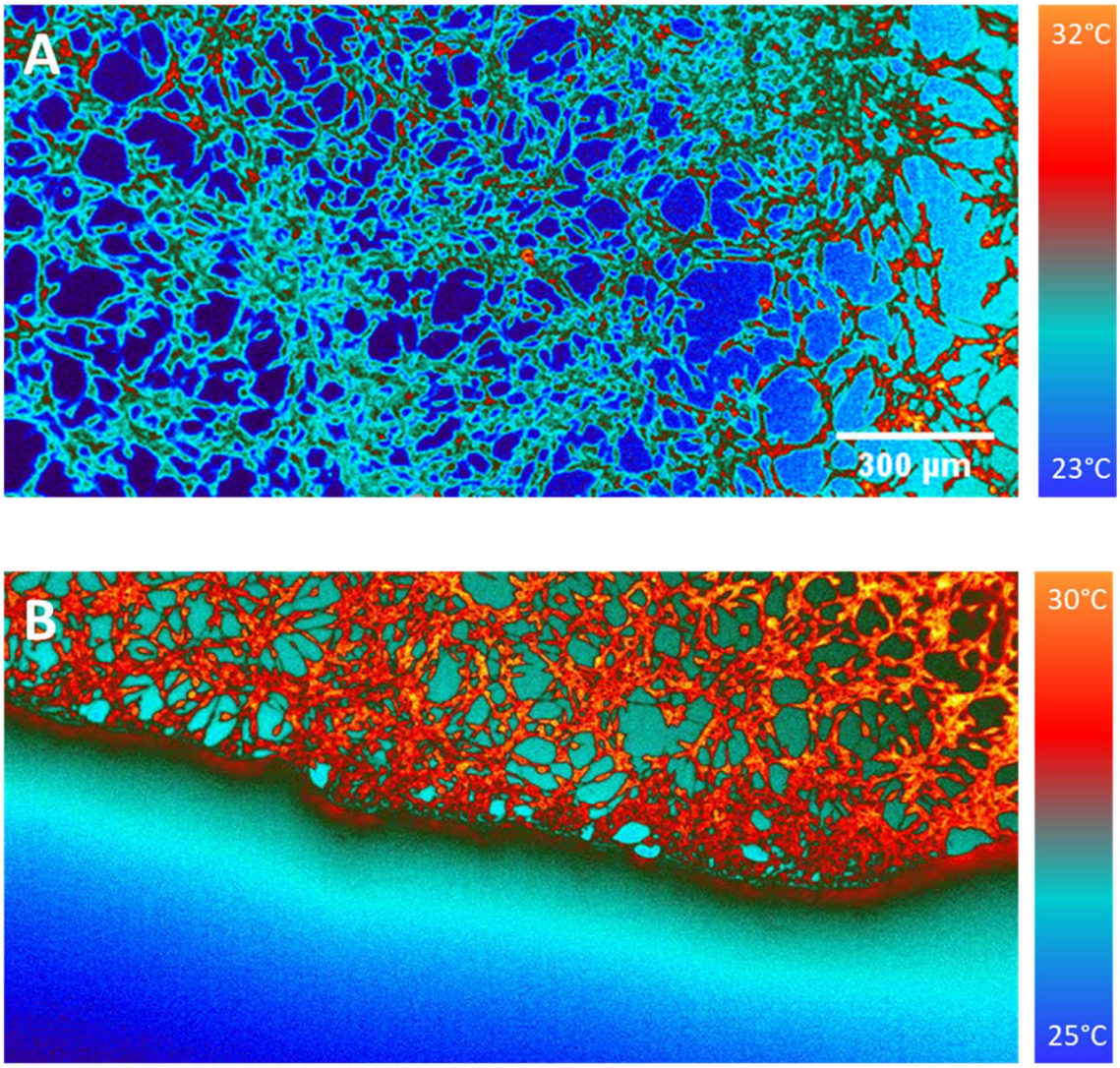

Figure S4: Thermal images of cultured 3T3 Fibroblasts. A) Cells imaged without any aqueous medium. B) Image of aqueous medium front advancing over cells. The absorption of water in the short-wave infrared is high, making cell culture medium difficult to image through with blackbody thermal contrast.

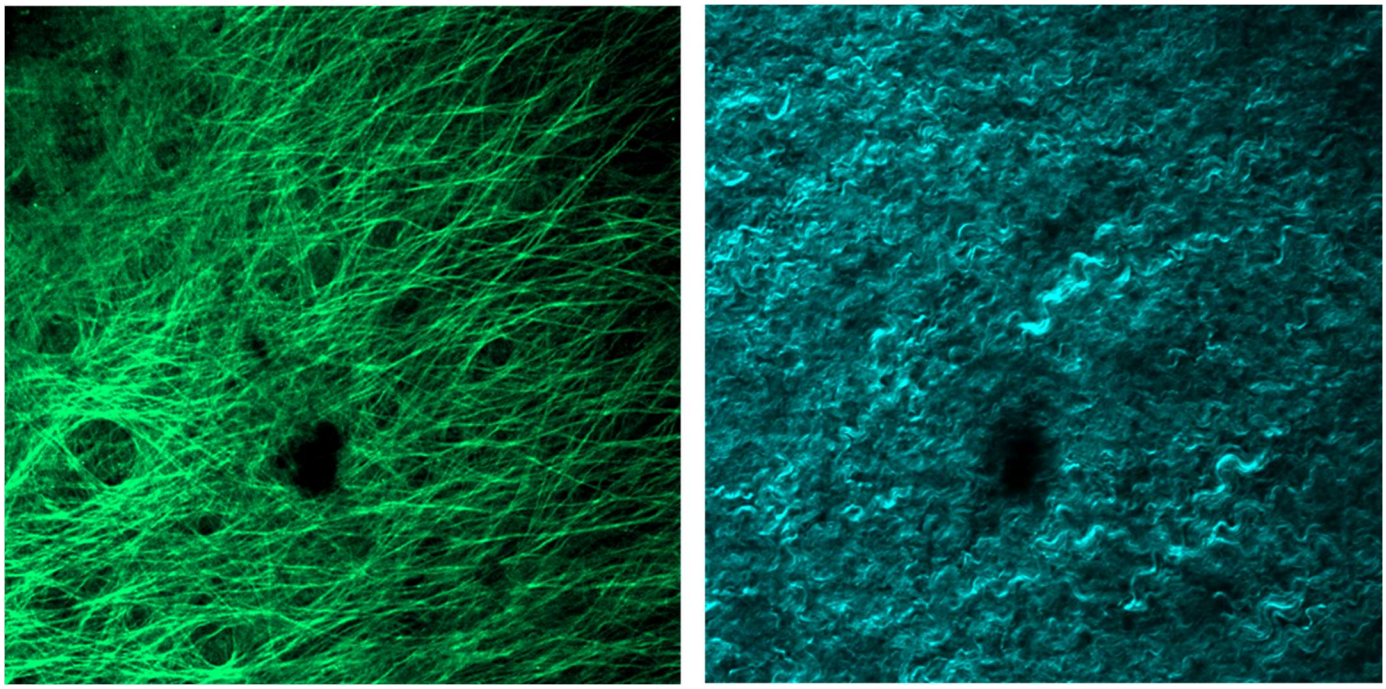

Figure S5: Porcine Mitral Valve imaging with endogenous autofluorescence from elastin (left) and collagen SHG (right). Image width is 520-µm.

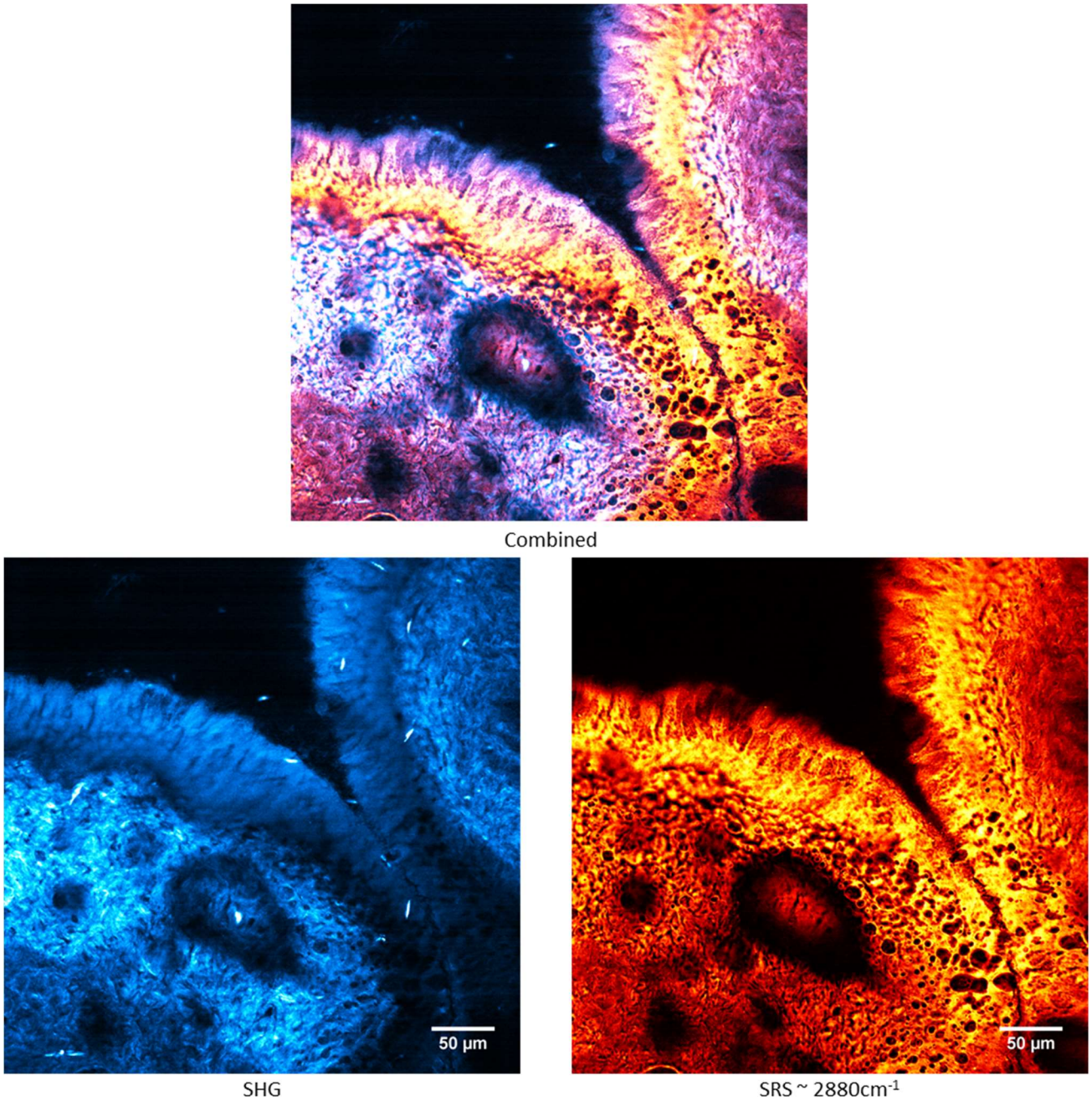

Figure S6: Simultaneous SHG (cyan) and SRS (2880-cm-1, lipid dominant resonance, orange) imaging of an unstained murine cervix unfixed frozen section. The stroma (dense in collagen) and epithelium are easily discernable based on relative concentrations on ratio of SHG and SRS signals. Blood vessels lamina propria are also visible with SHG contrast.

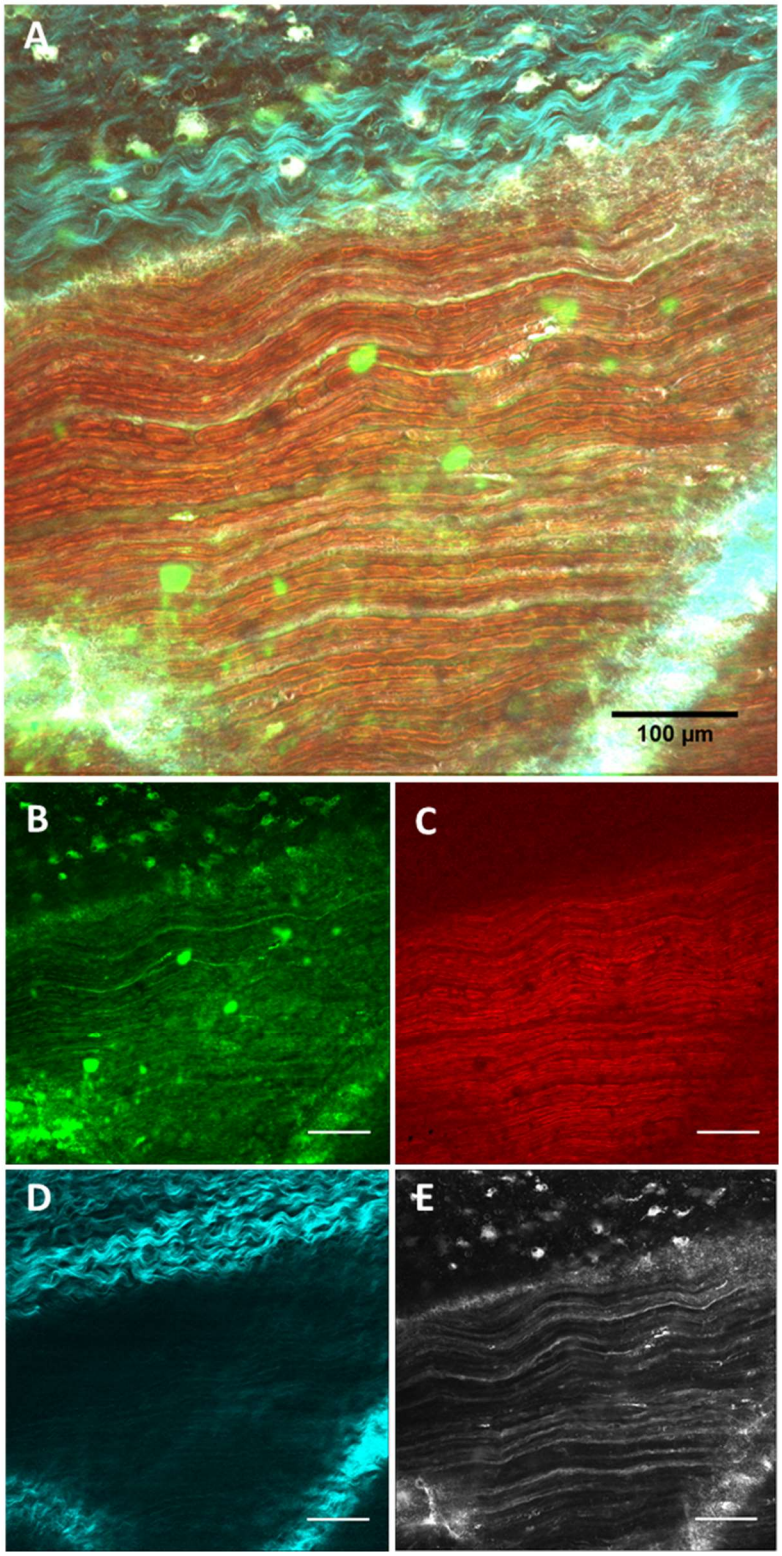

Figure S7: Composite multimode image of an ex vivo rat sciatic nerve. (A) CARS signal at 2927cm-1 (B, green), SRS signal at 2927cm-1 (C, red), SHG signal (D, cyan), and multiphoton fluorescence of FluoroMyelin Green (E, Grey). All scale bars are 100um.

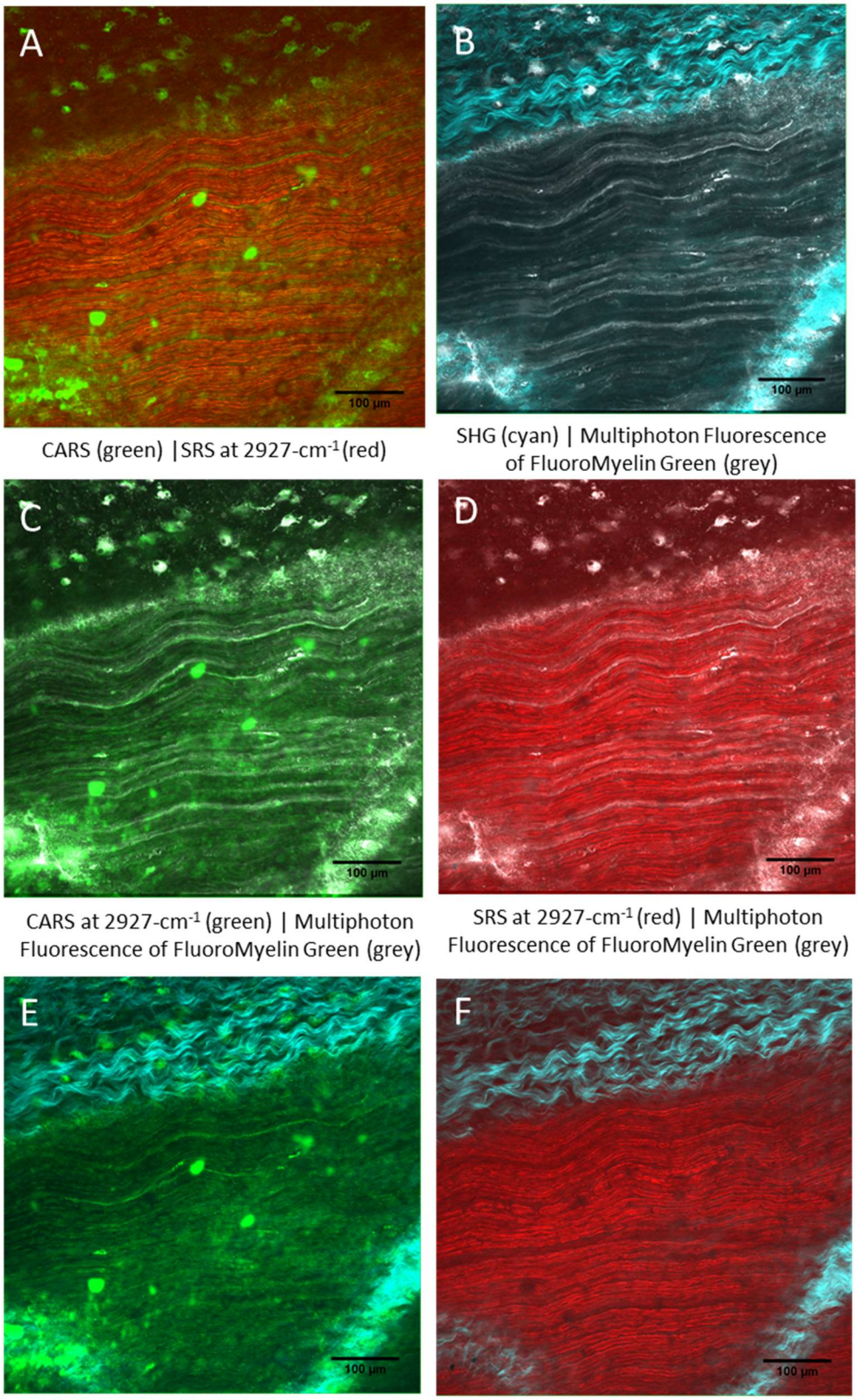

CARS (green) |SRS at 2927-cm^{-1} (red)

SHG (cyan) | Multiphoton Fluorescence of FluoroMyelin Green (grey)

CARS at 2927-cm^{-1} (green) | Multiphoton Fluorescence of FluoroMyelin Green (grey)

SRS at 2927-cm^{-1} (red) | Multiphoton Fluorescence of FluoroMyelin Green (grey)

CARS at 2927-cm^{-1} (greed) |.SHG (cyan)

SRS at 2927-cm^{-1} (red) | SHG (cyan)

723

Figure S8: Ex vivo rat sciatic nerve samples imaged with multimodal nonlinear imaging from Supp. Fig. 7. Two different modalities can be combined in different ways to visualize tissue structure.

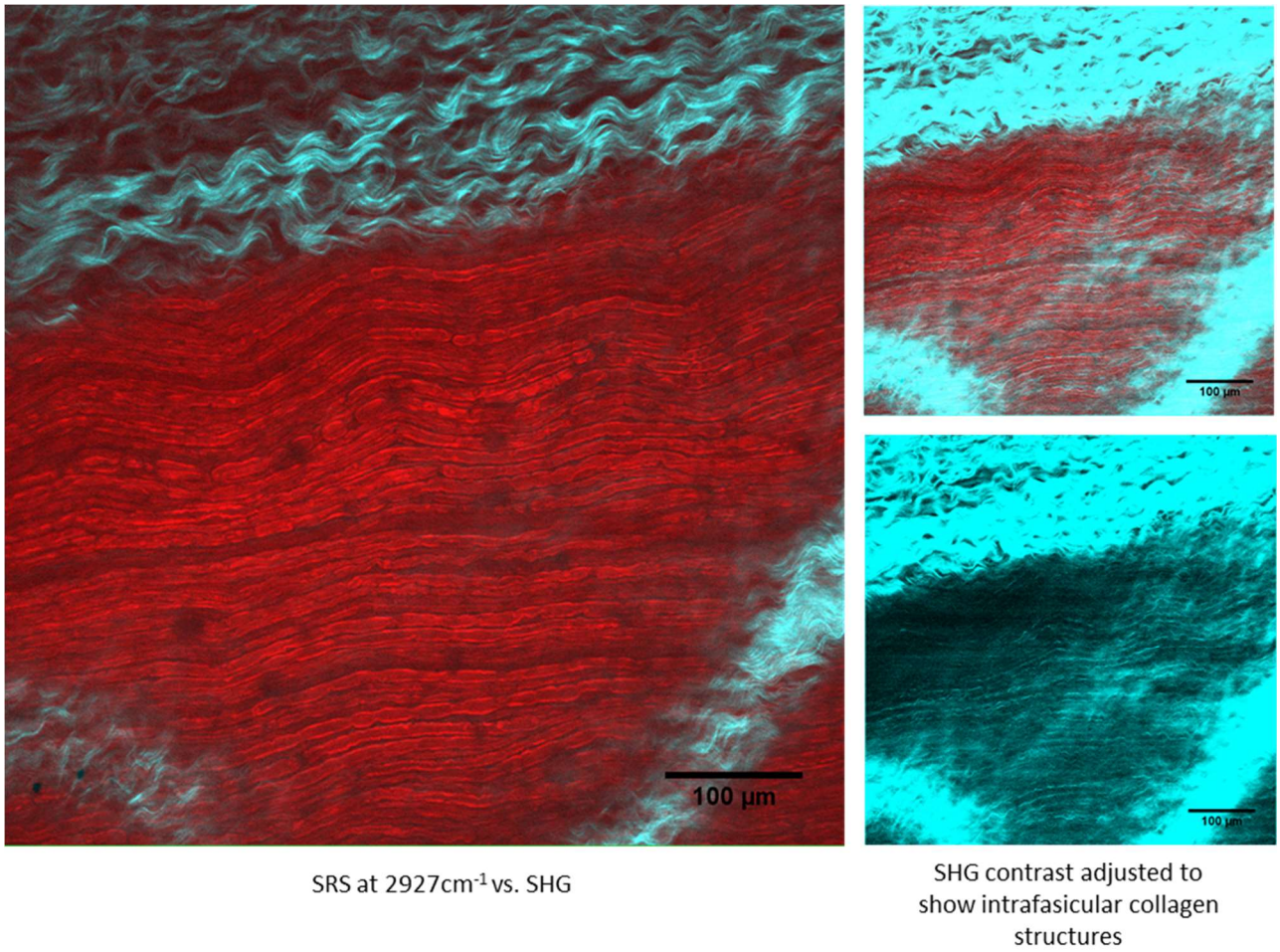

Figure S9: Supplementary Figure 9: Ex vivo rat sciatic nerve samples imaged with SRS (red, myelin at 2927cm-1) and SHG (cyan, collagen). Rescaled SHG images are shown to highlight intrafasicular collagen, which is in lower abundance and overall signal then epineurial collagen.